



Wiley Analytical Science Virtual Conference, 2021

20 April | 4pm-5pm CEST

Correlative Raman & SEM Imaging: Current Trends and Applications

Both Raman and SEM imaging are very well-established techniques in material research and geosciences. This virtual seminar will provide an introduction to basic principles of both techniques and their use in combination. Novel and innovative application examples from different fields of research will be presented to demonstrate the advantages of the correlative approach.

Key learnings:

- How to integrate Raman and SEM into one instrument
- How to differentiate materials with the same elemental composition
- Applications from materials and earth sciences requiring correlative, nondestructive analysis techniques for their full characterization
- The basics of confocal Raman and SEM imaging

Register here

Sponsored by



Wiley Analytical Science

Microscopic skin laceration segmentation and classification: A framework of statistical normal distribution and optimal feature selection

Farhat Afza¹ | Muhammad A. Khan² | Muhammad Sharif¹ | Amjad Rehman³

¹Department of Computer Science, COMSATS University Islamabad, Wah cant., Pakistan

²Department of Computer Science and Engineering, HITEC University, Museum Road, Taxila, Pakistan

³College of Business Administration, Al Yamamah University, Riyadh, Saudi Arabia

Correspondence

Amjad Rehman, College of Computer and Information Sciences, Prince Sultan University, Riyadh, Saudi Arabia.

Email: rkamjad@gmail.com

Review Editor: Paolo Bianchini

Abstract

Among precision medical techniques, medical image processing is rapidly growing as a successful tool for cancer detection. Skin cancer is one of the crucial cancer types. It is identified through computer vision (CV) techniques using dermoscopic images. The early diagnosis skin cancer from dermoscopic images can be decrease the mortality rate. We propose an automated system for skin lesion detection and classification based on statistical normal distribution and optimal feature selection. Local contrast is controlled using a brighter channel enhancement technique, and segmentation is performed through a statistical normal distribution approach. The multiplication law of probability is implemented for the fusion of segmented images. In the feature extraction phase, optimized histogram, optimized color, and gray level co-occurrences matrices features are extracted and covariance-based fusion is performed. Subsequently, optimal features are selected through a binary grasshopper optimization algorithm. The selected optimal features are finally fed to a classifier and evaluated on the ISBI 2016 and ISBI 2017 data sets. Classification accuracy is computed using different Support Vector Machine (SVM) kernel functions, and the best accuracy is obtained for the cubic function. The average accuracies of the proposed segmentation on the PH2 and ISBI 2016 data sets are 93.79 and 96.04%, respectively, for an image size 512 × 512. The accuracies of the proposed classification on the ISBI 2016 and ISBI 2017 data sets are 93.80 and 93.70%, respectively. The proposed system outperforms existing methods on selected data sets.

KEY WORDS

classification, feature extraction, fusion, lesion contrast, lesion segmentation, optimization, skin cancer

1 | INTRODUCTION

Skin cancer accounts for one-third of all types of cancer worldwide (Khan et al., 2018). In the United States, an estimated 87,000 cases of melanoma and more than 5 million cases of nonmelanoma have been reported (Rogers, Weinstock, Feldman, & Coldiron, 2015). An expected 53% new cases of melanoma have been diagnosed in the

United States since 2018 (<https://www.cancer.org/content/dam/cancer-org/research/cancer-facts-and-statistics/annual-cancer-facts-and-figures/2018/cancer-facts-and-figures-2018.pdf>). Accessed May 3, 2018; Kimball, 2018). About 90% of such cases are not only associated with the ozone layer but are also caused by solariums and the use of tanning (Koh, Geller, Miller, Grossbart, & Lew, 1996; Vasicek, Szpunar, & Manz-Dulac, 2018). The estimated number of diagnosed

new cases of melanoma in the United States since 2018 is 178,560, which comprises 87,290 noninvasive and 91,270 invasive cases. The number of estimated deaths since 2018 is 9,320, of which 3,330 are females and 5,990 are males (Siegel, Miller, & Jemal, 2018). A graphical representation is given Figure 1a, which shows that an estimated 192,310 new cases will be diagnosed as melanoma in 2019 whereas the estimated deaths are 7,230 in the United States (2019).

A considerable amount of money has been invested by the medical community for increasing the awareness of the population about skin cancer; however, this does not ensure safety. Therefore, it is essential to invest money in the advancement of the technologies that can be utilized for diagnosis processes at early stages (Barata, Celebi, & Marques, 2018). Doctors and dermatologists mostly utilize dermoscopy for the diagnosis of skin cancer; however, this process is time-consuming and expensive. Dermatologists mostly employ noninvasive methods such as the ABCD rule, 7-point checklist, optical imaging systems, and light scattering method (Khan et al., 2018; Nasir et al., 2018).

In the area of CV, several researchers have recently introduced computational methods for the automatic diagnosis and categorization of skin lesions (Kumar & Choudhury, 2019; Nida, Irtaza, Javed, Yousaf, & Mahmood, 2019; Saba, Al-Zahrani, & Rehman, 2012; Ullah et al., 2019). Skin lesions are broadly divided into two categories, that is, malignant and benign. In general, computational methods consist of the following steps, as shown in Figure 1b: First, lesions are enhanced in the preprocessing phase because good lesion contrast ensures correct segmentation. This is followed by the extraction of prominent features for efficient classification. Several hand crafted feature extraction techniques have been introduced in literature, such as HOG, point, geometric, SURF, Harlick, and Gabor. These features are subsequently classified using supervised learning methods such as

SVM, K-nearest neighbors (KNNs), decision trees (DTs), discriminant analysis, and neural networks (Alfed & Khelifi, 2017; Bakheet, 2017; Mahmoud, Abdel-Nasser, & Omer, 2018). The major purpose behind the extraction of these features is based on the shape of skin lesion. The each lesion type have a unique shape, color, and texture (Khan et al., 2019), therefore, the handcrafted features are well-suited as compare to deep learning-based features.

1.1 | Problem statement

Existing computational methods show improved performance. However, there are several challenges that must be overcome for achieving better performance. The major steps of Computer Aided Design (CAD) systems are shown in Figure 1. The presence of artifacts such as bubbles, low contrast, and hairs degrades the segmentation accuracy, which later diminishes the classification accuracy. The good contrast stretching is a guarantee of better segmentation accuracy. In the segmentation step, attains several issues like lesion shape, irregularity, and the occurrence of a lesion in the border region. These challenges diminish overall segmentation performance. The prominent feature extraction is another major issue because of the irrelevant and redundant features affects classification accuracy. The major challenges which we handle in this work are the similarity between a lesion and healthy region, lesion texture, shape, and selection of best feature sets.

1.2 | Contributions

In this article, we propose a new automated system that applies a new lesion contrast enhancement technique and then performs segmentation. After segmentation, we extract three types of features, that is, optimized color (OCL) features, optimized HOG (OHOG), and GLCM

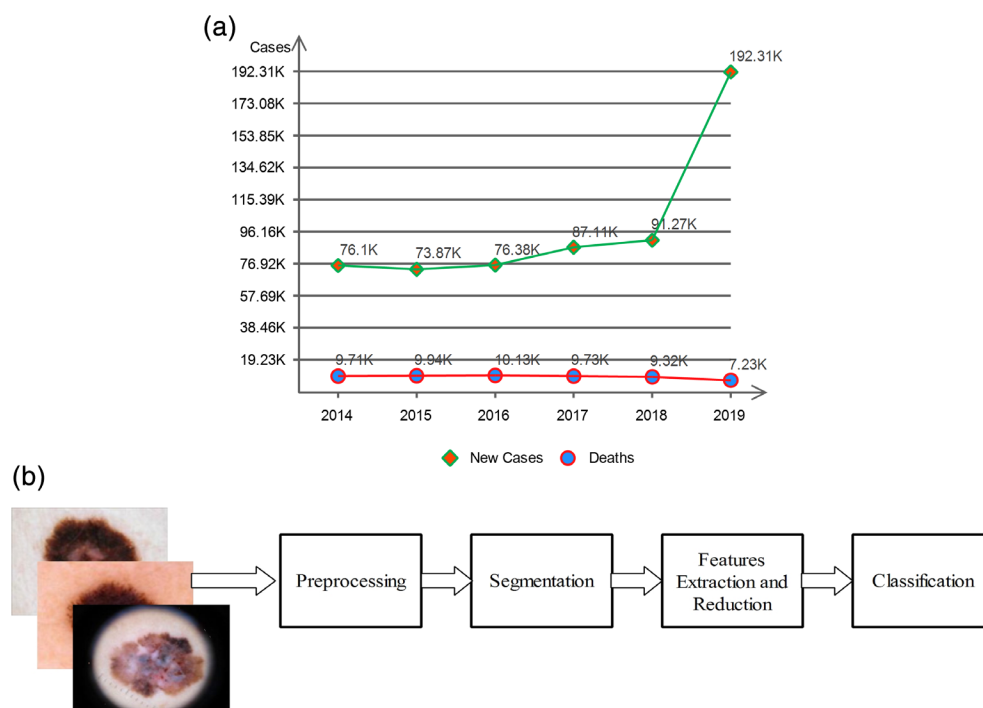


FIGURE 1 (a) Skin cancer facts and figures. (b) General steps of any automated system for skin lesion [Color figure can be viewed at wileyonlinelibrary.com]

texture features. These features are subsequently fused in one matrix through simple concatenation, and the best features are selected based on the partial least square regression theory. The selected features are finally fed to an SVM of RBF kernel function for classification. The major contributions of this study are provided below.

1. A local contrast controlled by brighter channel (LCcbBC) technique is proposed for lesion contrast stretching. The proposed technique clearly differentiates between lesion and healthy regions.
2. A statistical normal distribution (SND) approach is proposed based on quartile deviation (QD) and mean absolute deviation around median (MADaM). The approach is implemented on LCcbBC-enhanced images. Finally, QD and MADaM binary images are fused by utilizing the multiplication law of probability (MLoP).
3. Optimized OCL, OHOG, and GLCM texture features are calculated. Then, covariance-based fusion is performed, in which strong covariance (close to 1) features are add in a fused vector.
4. A binary grasshopper optimization (BGO) algorithm is implemented for selecting the best features based on current feature position, updated feature position, and a fitness function.

2 | RELATED WORK

The segmentation and classification of skin lesions, such as melanoma, has been a challenging task in past decades owing to poor contrast between lesions and enclosing skin, irregular skin borders, artifacts, and insufficient number of features. Yuan, Chao, and Lo (2017) presented the Jaccard distance with a deep learning model for segmentation. The presented model does not aspect on the earlier information of the data. A Jaccard-distance-based novel loss function was introduced for lesion segmentation. This method was evaluated on the ISBI 2016 and PH2 data sets, and it showed efficient performance.

Mirikhariji and Hamarneh (2018) introduced a star-shape-prior-based technique for skin lesion segmentation that utilized Faster Convolutional Neural Networks (FCNN)s. The technique was based on semantic segmentation because Convolutional Neural Networks (CNN)s are the first choice for performing pixel-wise lesion segmentation. The method was evaluated on the ISBI 2017 data set, and it achieved better accuracy among 21 participating groups. Navarro, Escudero-Vinolo, and Bescos (2018) presented an automatic CAD system for skin lesion classification. The authors described that sound feature extraction was a key factor for the performance of CAD systems. A superpixel-based technique was adopted by the authors for lesion segmentation. Further, a registration process was utilized to evaluate the presented approach on the ISIC 2017 data set, and the approach achieved good accuracy. Nasir et al. (2018) presented a CAD system, which is based on the integration of five primary steps. Contrast stretching was improved in the first step, and segmentation was performed in the second step using a hybrid approach. Three types of important features were extracted and fused by employing a serial-based approach. Subsequently, an entropy controlled selection approach was implemented to select the best features for the final

classification. The system was evaluated on the PH2 data set, and it achieved a classification accuracy of 97.5%. Khan et al. (2018) introduced a probabilistic segmentation and best feature selection technique for melanoma classification. A uniform-and-normal-distribution-based approach was introduced for lesion segmentation. Then, multilevel features were extracted, and a parallel approach was utilized for feature fusion. A distance-and-variances-based selection approach was also designed for best feature selection, which were finally classified by an SVM. The PH2, ISBI, and ISIC data sets were utilized for evaluating the approach, which exhibited excellent performance. Mahmoud et al. (2018) presented a CAD system based on texture features. The system consisted of four major steps, that is, hair removal, noise removal, features extraction, and finally classification. Gabor, texture, GLCM, HOG, and LBP features were extracted and fed to the classifier for the final classification. The results revealed that HOG performed more efficiently compared to other feature extraction methods.

Dey, Rajinikanth, Ashour, and Tavares (2018) implemented a social group optimization approach to measure the skin lesion in the dermoscopic scans. In the implemented method, Otsu and Kapur-based thresholding is performed and later level set theory and active contour-based segmentation is performed. The implemented method outperforms on the selected data sets in terms of dice and Jaccard index. Masood and Al-Jumaily (2018) presented a skin lesion segmentation based on clustering and level set theory. In the start, Fuzzy C Means-based initialized coarse segmentation and later refined through level set algorithm. The experiments are performed on 150 images and achieved an accuracy of 87.66%.

The above-described methods show that there is a gap between skin lesion segmentation and sufficient feature selection. In the segmentation step, shape, color, and the irregularity of lesions affect segmentation accuracy. Moreover, a good contrast stretching approach ensures correct lesion segmentation and prominent feature extraction. Furthermore, best-feature-selection techniques minimize computational cost and improve overall system accuracy.

3 | PROPOSED METHOD

In this section, we describe the automated CAD system proposed for the segmentation and recognition of skin cancer from dermoscopy images. The proposed system includes the following five major steps: (a) lesion preprocessing based on LCcbBC; (b) implementation of QD and MADaM on LCcbBC-enhanced images and image fusion based on the simple MLoP; (c) extraction of OCL, OHOG, and GLCM texture features; (d) fusion of extracted features, and particle swarm optimization for optimal feature selection (OFS); (e) final recognition using one versus one approach. The overall structure of proposed system is shown in Figure 2.

3.1 | LCcbBC enhancement

In computer vision, medical imaging is an important research area for the diagnosis of infections or cancer. Image enhancement or

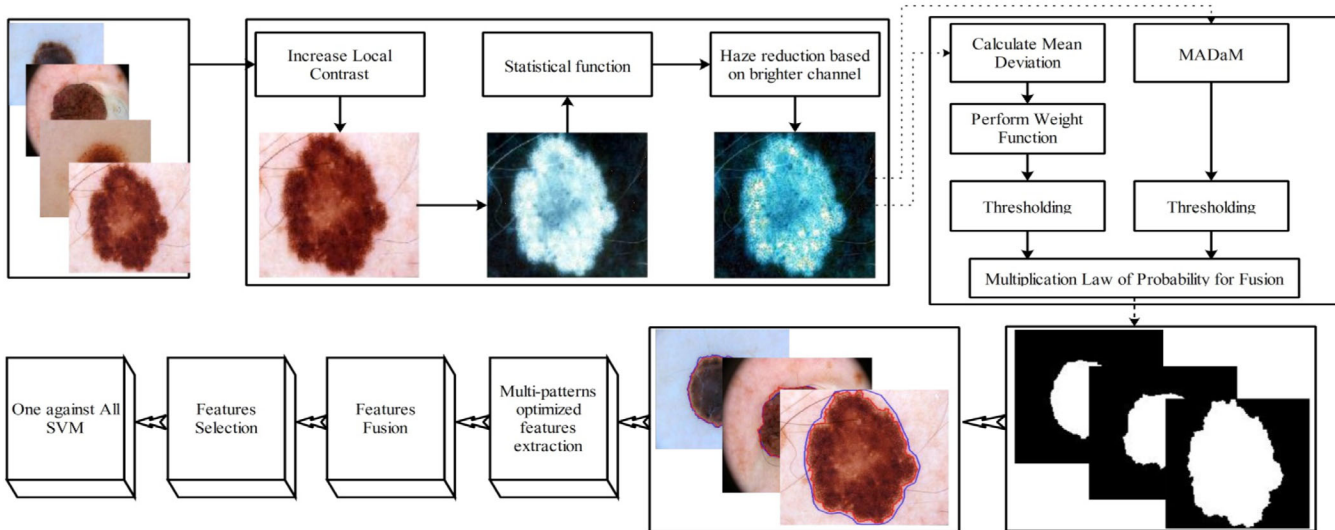


FIGURE 2 Overall structure of proposed skin lesion segmentation and classification [Color figure can be viewed at wileyonlinelibrary.com]

contrast stretching is the first step in computer-based diagnostic systems for determining the orientation of a lesion part in a dermoscopic image. This step is highly essential for improving lesion contrast and removing noise and other factors, such as bubbles and hairs, which affect segmentation accuracy. The color similarity between healthy regions and lesions and low contrast lesions also affect segmentation and feature extraction. Therefore, in this work, we propose a contrast stretching method named LCcbBC, which successfully searches for abnormal regions in a given image. The proposed LCcbBC method consists of the following three steps: (a) increase local contrast; (b) apply a statistical function to a local contrast image; (c) reduce haze based on brighter channel selection. The detailed description of each step is provided below.

Let $O(p, q)$ denotes original RGB dermoscopy image of dimension $N \times M$, where N denotes length of rows pixels and M denotes the length of column pixels. Let Q denotes the local area of $O(p, q)$ which is defined as $(2x + 1)(2x + 1)$ over window size p and q , where $p, q \in \text{rows}$ and column pixel values. Then calculate local mean and standard deviation of $O(p, q)$ as follows:

$$\mu(p, q) = \frac{1}{(2x + 1)^2} \sum_{p=1}^n \sum_{q=1}^n O(p, q) \quad (1)$$

$$\sigma^2(p, q) = \frac{1}{(2x + 1)^2} \sum_{p=1}^n \sum_{q=1}^n [O(p, q) - \mu(p, q)]^2 \quad (2)$$

$$\sigma(p, q) = \sqrt{\sigma^2(p, q)} \quad (3)$$

where $\mu(p, q)$ denotes local mean value for pixels (p, q) , $\sigma^2(p, q)$ is variance value, and $\sigma(p, q)$ is a standard deviation. Suppose, $\xi(p, q)$ describe the improve value of $O(p, q)$, then the lesion contrast is enhanced by following function.

$$\xi(p, q) = \mu(p, q) + \phi(p, q)[O(p, q) - \mu(p, q)] \quad (4)$$

where $\xi(p, q)$ represents the improved local contrast image, $\phi(p, q)$ denotes the contrast gains and its range is more than 1. The $\xi(p, q)$ image is further improved by implanting a statistical function as given below:

$$F(p, q) = \mu(p, q) + C \times \frac{O(p, q) - \mu(p, q)}{\sigma(p, q)}, \text{ where } C = 4 \quad (5)$$

After that, we perform a dehaze reduction algorithm based on brighter channel. Haze reduction is commonly high desired problem in computer vision applications. The reduction algorithm correctly removes the visibility problem in the input images and makes object clearly visible in the image. For enhanced image, $F(p, q)$, the brighter channel is defined by below given function.

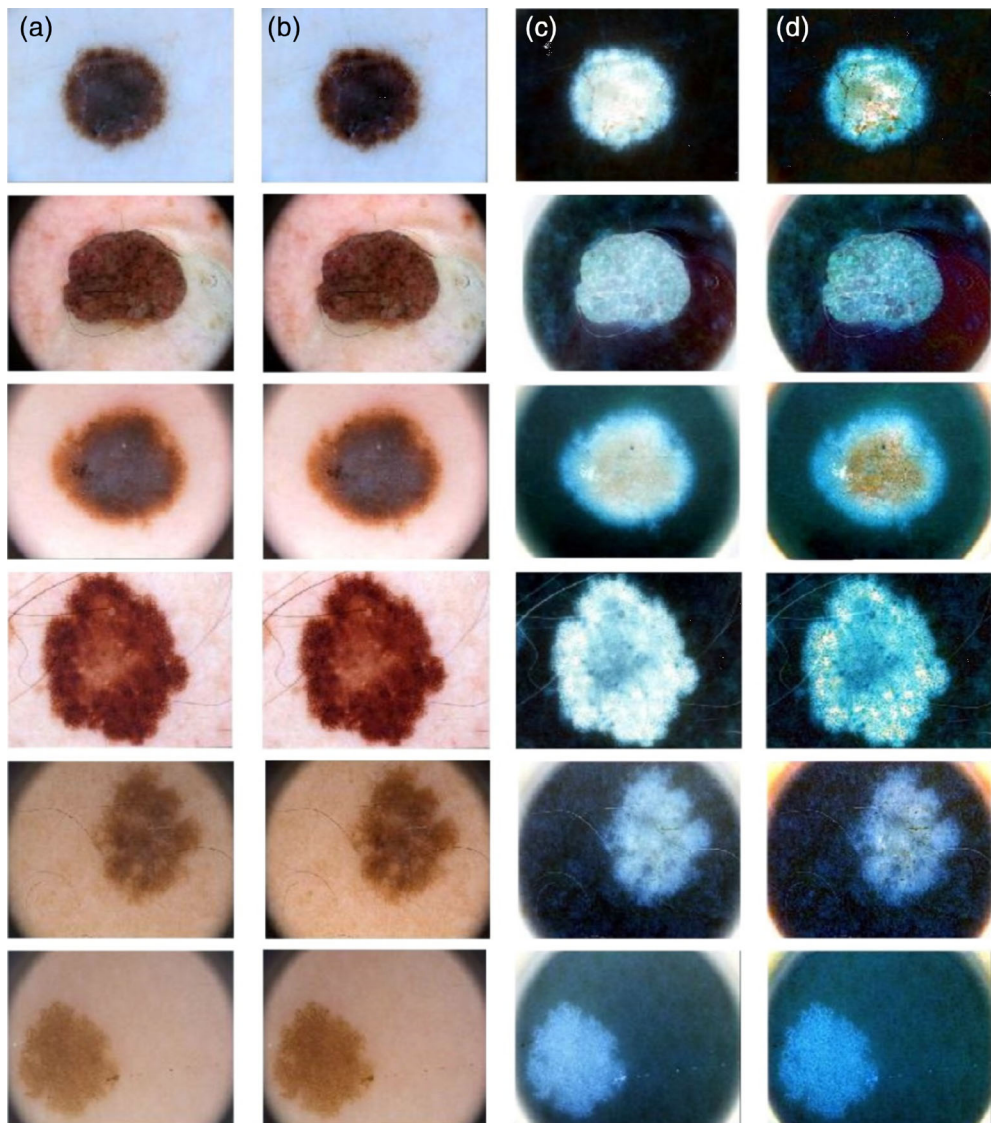
$$F^b(p, q) = \max_{y \in \Delta(x)} \left(\max_{\alpha \in \{R, G, B\}} F(p, q) \right) \quad (6)$$

where $\Delta(x)$ denotes the local patch of window size 10×10 , $F^b(p, q)$ represents haze reduction image, α denotes the max operator from R, G, and B. The above function highlight the lesion region and dark the healthy parts. The LCcbBC enhancement effects as shown in Figure 3, which explains that (a) original images, (b) local contrast enhancement images, (c) statistical stretching function images, and (d) brighter contrast haze reduction images with brighter lesions.

3.2 | Segmentation

Lesion segmentation is an essential parameter in CAD systems for diagnosis processes. Incorrect segmentation affects classification accuracy (Khan et al., 2019; Norouzi et al., 2014). Even a good classifier performs poorly when the segmentation process is not performed accurately, and a simple classifier exhibits superior performance in the

FIGURE 3 Local contrast controlled by brighter channel contrast stretching effects on ISBI 2016 and ISBI 2017 data set images. (a) Original image, (b) local contrast enhancement, (c) statistical stretching function, and (d) brighter contrast haze reduction [Color figure can be viewed at wileyonlinelibrary.com]



case of correct segmentation. Several factors degrade segmentation accuracy, such as the quality of lesions, borders, lesion irregularity, and diameter. Well-known segmentation algorithms, such as Otsu and active contour models, perform efficiently when the contrast difference between lesion and healthy regions is satisfactory (Vesal, Patil, Ravikumar, & Maier, 2018). In this article, we propose an SND-based segmentation technique based on QD and MADaM. Initially, a QD value is calculated from an enhanced image and input to a fitness function. The fitness function returns a single value, which is input to a threshold function for a binary image. Second, MADaM is calculated, which returns a single value, that is, utilized for the threshold function. The threshold function returns a binary image. Subsequently, the MLoP is implemented for the fusion of both binary images. The major aim of the fusion process is to obtain a new improved image that is superior to the single binary image. Mathematically, the SND segmentation technique is defined below:

Let $p_i q_j$ denotes the pixels values of enhanced RGB image $F^b(p, q)$ of dimension $N \times M$, then for computation of QD, we need σ which is calculated as follows:

$$\sigma(i,j) = \sqrt{\sum_{i=1}^n \sum_{j=1}^n \frac{[F^b(i,j) - \mu(i,j)]^2}{\lambda}} \quad (7)$$

where λ denotes the total number of pixel values of an image and $(i, j) \in p, q$. Thereafter, put the value of σ into QD formula as given:

$$Q_D = 0.6745\sigma \quad (8)$$

The Q_D formula is computed by normal distribution and its proof is given below:

Suppose, Q_1 and Q_3 denotes lower and higher quartiles and μ is a mean value which is initialized as 0. Then equations of both quartiles are defined by addition and difference of mean value as shown in Figure 4.

$$Q_1 = \mu - 0.6745\sigma, Q_3 = \mu + 0.6745\sigma \quad (9)$$

$$Q_D = \frac{Q_3 - Q_1}{2} \quad (10)$$

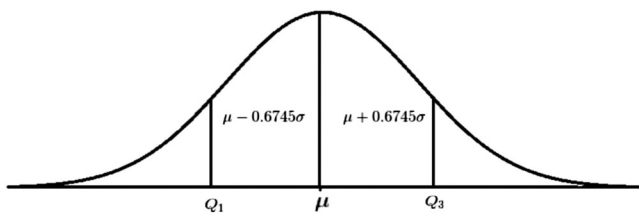


FIGURE 4 Normal representation for computation of quartile deviation

Putting the formulation of Q_1 and Q_3 into equation and become as:

$$Q_D = \frac{\mu + 0.6745\sigma - \mu + 0.6745\sigma}{2} \quad (11)$$

$$Q_D = \frac{2(0.6745\sigma)}{2}, Q_D = 0.6745\sigma \quad (12)$$

where σ denotes the standard deviation.

After computation of Q_D , put the value of Q_D into a fitness function as given below which return a value that is utilized in final threshold function. The value which is return by fitness function F_n is correctly identify the lesion and healthy pixels.

$$F_n = C \times \frac{(F^b(p,q) - Q_D)}{\sigma} \quad (13)$$

$$T = \begin{cases} 1 & \text{if } F^b(p,q) \geq Q_D \\ 0 & \text{Otherwise} \end{cases} \quad (14)$$

where C is a constant value and initialized $C = 2$. The threshold function T explains that if enhanced image pixel values are greater than F_n , its represents as lesion, otherwise healthy region. The binary image after performing threshold function is represented by $Q_D(p, q)$ of size $N \times N$.

After thresholding, a MADaM is also computed from enhanced RGB image. The major aim of MADaM approach is to minimize the segmentation error rate. The MADaM offers to directly measure the scale of pixel values. The MADaM is formulated by below expression:

$$D_{\text{med}} = E|F^b(p,q) - M_d| \quad (15)$$

where M_d denotes the median value of image $F^b(p, q)$ which is mathematically explains as $M_d = \frac{(n+1)}{2}$ and n denotes the total number of image pixels. In normal distribution, the median minimize the average absolute distance so

$$D_{\text{med}}(p,q) = E|F^b(p,q) - M_d| = 2 \text{COV}(F^b(p,q), \Delta_0) \quad (16)$$

$$\Delta_0 = \begin{cases} 1 & \text{if } F^b(p,q) \geq M_d \\ 0 & \text{Otherwise} \end{cases} \quad (17)$$

Finally, both $Q_D(p, q)$ and $D_{\text{med}}(p, q)$ binary images are fused by multiplication law of probability (MLoP). The MLoP theorem combine those pixels whose are common between both images. The major property of MLoP is the equal dimension of both binary images. The expression of MLoP is defined as:

Let S denotes a sample space, and A denotes the pixels of binary images, where $A \in Q_D(p, q)$, $D_{\text{med}}(p, q)$, and $P(A) > 0$. Then, $P(A_1|A_2) = P\left(\frac{A_1 \cap A_2}{A_2}\right)$. Further simplify $P(A_1|A_2)$, we obtain an expression:

$$P(A_1 \cap A_2) = P(A_1|A_2)P(B)$$

$$P(A_1 \cap A_2 \cap A_3 \dots \cap A_m) = P(A_1)P(A_2|A_1)P(A_3|A_1 \cap A_2) \dots P(A_m|A_1 \cap A_2 \cap A_3 \dots \cap A_{m-1}) \quad (18)$$

The segmentation results of proposed SND approach is shown in Figure 5a.

3.3 | Features extraction

In the domain of image processing, medical imaging, and machine learning, a large amount of data is generated and stored. However, several factors exist in stored data, such as noise and irrelevant and redundant information. These factors affect system performance in terms of accuracy and computational cost. Feature extraction is an essential step in automated machine learning systems (Khan et al., 2017; Sharif et al., 2017). Extracted features contain redundant and irrelevant information owing to the above-mentioned factors. High-dimensionality feature vectors are another challenging issue for CAD systems in medical imaging (Akram, Khan, Sharif, & Yasmin, 2018). In recent years, researchers have overcome this challenge by utilizing reduction and best feature selection algorithms. However, these algorithms experience problems, for example, reduction methods minimize the prediction level and the number of observations. In this work, we extract OHOG, OCL, and GLCM features. The extracted features are optimized by a statistical theorem named principal component analysis (PCA) controlled variances (PCAcV) and fused based on the covariance method. Finally, optimal features are selected by a PSO algorithm. The selected features are classified by an ensemble classifier for the desired output, as flow demonstrated in Figure 6. A brief description of each step is provided below.

3.3.1 | OHOG features

HOG features represent the local information of an object in an image, such as edge information. In this work, we implement HOG features and then optimize them using the PCAcV approach. The HOG features are extracted from segmented lesion images. Before computing HOG descriptors, images are resized to 56×120 , and then, features are calculated from 16×16 local regions. Initially, edge gradients and orientation are computed for each pixel value, which are contained in local regions. Then, the Sobel filter is employed to obtain the orientation and

FIGURE 5 Proposed segmentation results on ISBI 2016 data set. (a) Enhanced RGB image, (b) proposed segmented lesion, (c) mapped on original RGB, and (d) compared groundtruth and proposed segmented (blue line denotes ground truth and red line proposed segmented) [Color figure can be viewed at wileyonlinelibrary.com]

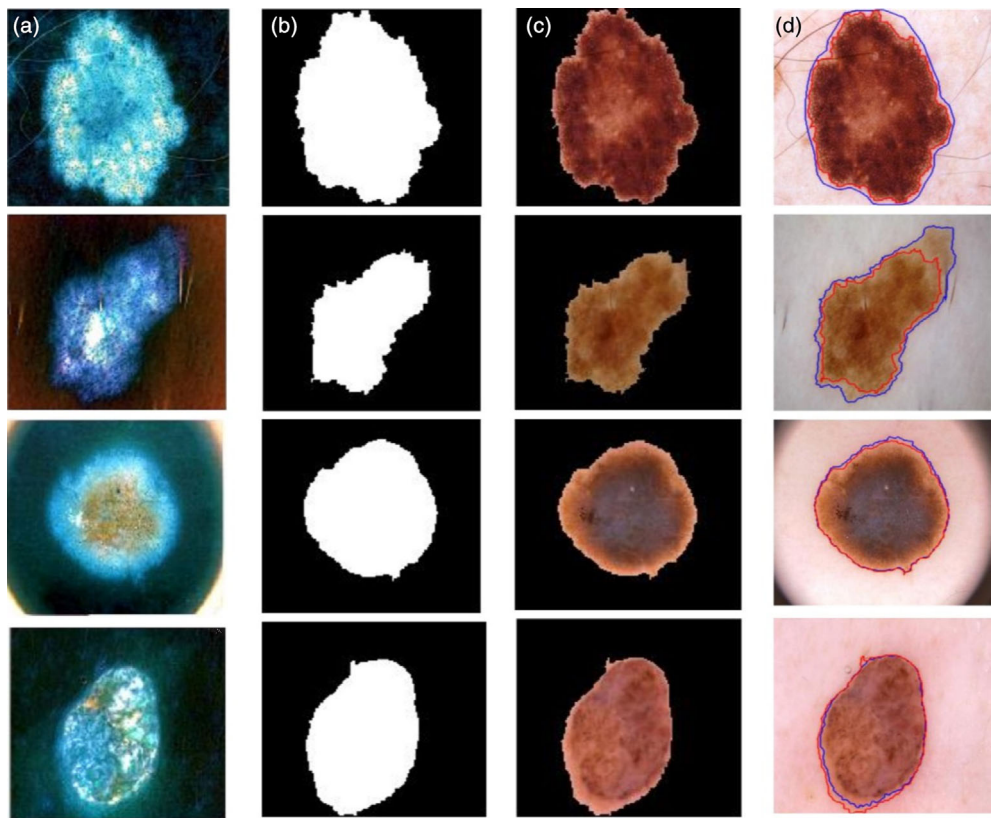
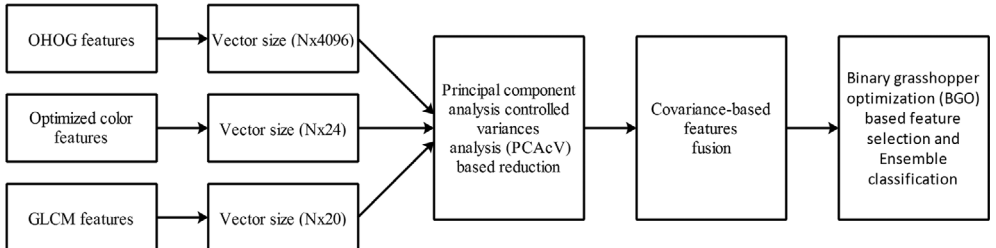


FIGURE 6 Representation of feature extraction and selection process



gradient information. The magnitude and orientation of gradients are computed using the x and y directional gradients D_x and D_y .

$$m = \sqrt{D_x^2 + D_y^2} \quad (19)$$

$$\theta = \begin{cases} \tan^{-1}\left(\frac{D_y}{D_x}\right) - \pi & \text{if } D_x < 0, D_y < 0 \\ \tan^{-1}\left(\frac{D_y}{D_x}\right) + \pi & \text{if } D_x < 0 \text{ and } D_y > 0 \\ \tan^{-1}\left(\frac{D_y}{D_x}\right) & \text{Otherwise} \end{cases} \quad (20)$$

After computation of gradients, local regions are divided into small cells of size 8×8 pixels. Then histogram is computed for each local pixels based on bin size 8 and return a feature vector of size $8 \times (8 \times 8) = 512$ and from all grids it become 4,096. The HOG features are represented by $F_H(i)$. Thereafter, proposed PCAcV approach is implemented on extracted HOG vector $F_H(i)$. The aim of PCAcV approach is to select the strong features. The aim of PCAcV approach is to

removes the redundant and irrelevant information in feature vector $F_H(i)$.

Theorem 1: PCAcV

PCA is a well-defined technique of dimensionality reduction in the domain of computer vision and pattern recognition. In this work, we utilized PCA to compute the principle score (PS) values of extracted features. Subsequently, variance is calculated from the computed PS values and the best features are selected based on the minimum variance. Mathematically, PCAcV is formulated as follows:

Let $\{h_i | i = 1, 2, 3, \dots, N\}$ be a set of N dimensional HOG feature vector, where $h_i \in F_H(i)$. A projection matrix U is implemented for computation of PS as follows:

$$P_s(i) = U^T (h_i - \bar{h}) \quad (21)$$

where \bar{h} denotes mean value of matrix defined as $\bar{h} = \frac{1}{N} \sum_{i=1}^N h_i$. The projection matrix U is obtained by solving the Eigen equations of the covariance matrix Σ . The covariance matrix Σ is formulated as:

$\sum U = U\Lambda$, ($UU^T = I$), where I denotes the identity matrix.

$$\sum = \frac{1}{N} \sum_{i=1}^N (h_i - \bar{h})(h_i - \bar{h})^T \quad (22)$$

Thereafter, variance is computed from PS vector $P_s(i)$ as:

$\sigma^2 = \frac{1}{N} \sum_i^N (s_i - \bar{s})$, where $s_i \in P_s(i)$, N denotes the total number of PC features, and \bar{s} denotes the expected mean value. Finally, sort all variance features into ascending order and selects top 50% features which are optimal as compare to remaining features. The selected features are save into a matrix represented by $F_{Hs}(i)$.

3.3.2 | OCL features

In this step, initially color features are extracted using enhanced haze reduction image $F^b(p, q)$. Two types of color spaces are utilized for color features extraction as RGB and HSV. Four metrics are computed for each channel of selected color spaces. The extracted metrics are cluster prominence, cluster shade, visibility, and root mean square (RMS) contrast. The major aim of computed these pixels to make the difference between healthy and lesion pixels. Mathematically, these metrics are computed as:

$$CP = \sum_{i=0}^{m-1} \sum_{j=0}^{n-1} \{i + j - \phi^{\mu_x} - \phi^{\mu_y}\}^4 P(i,j) \quad (23)$$

$$CS = \sum_{i=0}^{m-1} \sum_{j=0}^{n-1} \{i + j - \phi^{\mu_x} - \phi^{\mu_y}\}^3 P(i,j) \quad (24)$$

$$Vs = \frac{E_{\max} - E_{\min}}{E_{\max} + E_{\min}} \quad (25)$$

$$RMS = \sqrt{\frac{1}{mn} \sum_{i=1}^m \sum_{j=1}^n (E_{ij} - \bar{E})^2} \quad (26)$$

where E_{\max} and E_{\min} denotes the maximum and minimum pixel values of extracted channels. CP denotes the cluster prominence, CS denotes the cluster shade, Vs represents visibility, and RMS denotes the root mean square contrast, respectively. These metrics are computed from each color channel and concatenate by simple serial methods which gives a resultant vector of size $K \times 24$ denotes by $F_C(i)$, where K represents the total number of images that are utilized for color features extraction. Finally, proposed theorem 1 PCAcV selection method is applied on color vector $F_C(i)$ and selects the top 50% features represented by $F_{Cs}(i)$.

3.3.3 | GLCM texture features

Texture features are extremely important in the domain of medical imaging for extracting the surface information of a disease region. In skin cancer, malignant and benign regions have distinct textures;

therefore, texture information must be calculated for classification. In this work, we extract GLCM features from binary images. The GLCM features measure the major image properties such as correlation and visual information (Ondimu & Murase, 2008). Five important parameters are calculated, that is, correlation, homogeneity, energy, contrast, and entropy from each given image (Xian, 2010). These parameters are calculated from four different angles, that is, 30° , 45° , 60° , and 90° which gives a resultant vector of dimension $N \times 20$, where N denotes the number of images utilized for feature extraction. The GLCM feature vector is represented by $F_G(i)$.

3.4 | Features fusion

Let F_1 , F_2 , and F_3 be three set of extracted feature vectors on sample space Δ , where $F_1 \in F_{Hs}(i)$, $F_2 \in F_{Cs}(i)$, and $F_3 \in F_G(i)$. Let $f_i \in F_1$, $f_j \in F_2$, and $f_k \in F_3$, then $f_i, f_j, f_k \in \Delta \subset R^N$. The corresponding vectors are $u = F_1 \subset R^m$, $v = F_2 \subset R^n$, and $w = F_3 \subset R^o$, respectively. Given that three feature matrix on sample space Δ are represents by $X \in R^{m \times t}$ for $F_1 Y \in R^{n \times t}$ for F_2 and $Z \in R^{o \times t}$. Initially, compute the covariance among indexes i, j , and k for all feature vectors.

Let i, j , and k are indexes for feature vectors X , Y , and Z , respectively and their mean values are \bar{x} , \bar{y} , and \bar{z} , that are calculated as:

$$\bar{x} = \frac{\sum_{i=1}^m X_i}{m}, \bar{y} = \frac{\sum_{j=1}^n Y_j}{n}, \text{ and } \bar{z} = \frac{\sum_{k=1}^o Z_k}{o} \quad (27)$$

Thereafter, covariance is computed as follows:

$$CV(I) = \frac{\sum_{i=1}^m \sum_{j=1}^n \sum_{k=1}^o (X_i - \bar{x})(Y_j - \bar{y})(Z_k - \bar{z})}{(m-1)(n-1)(o-1)} \quad (28)$$

After computing covariance among all extracted features of three vectors, selects those features whose covariance value is near to 1 and ignore remaining features. The selection of covariance features are done by following function:

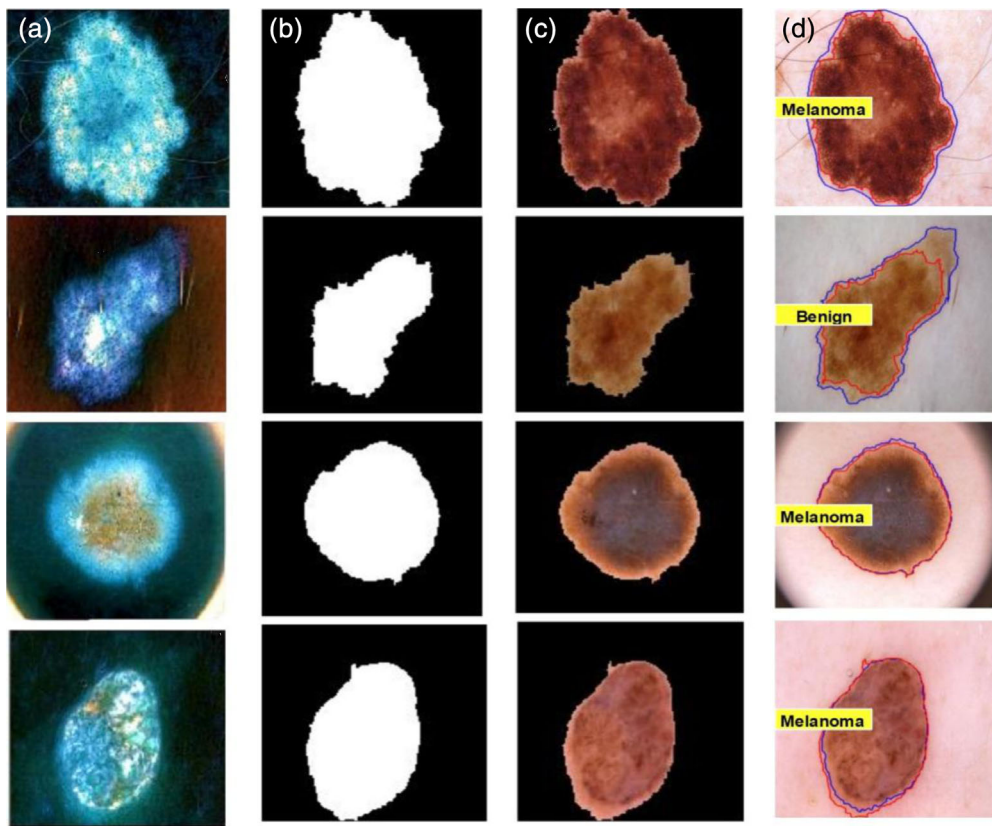
$$\xi(k) = \begin{cases} S(k) & \text{if } CV(I) \geq \varphi \\ N(k) & \text{if } CV(I) < \varphi \end{cases} \quad (29)$$

where $\xi(k)$ denotes the fused feature vector and depend on $S(k)$, where $S(k)$ represents the selected fused features vector through thresholding function defined in above equation and φ represents the value that are near to 1. The size of fused vector is depend on the covariance value φ . Later step, best features are selected from fused vector $\xi(k)$.

3.5 | Features selection

In wrapper feature selection methods, the selection of the best features is a challenging task. A lot of feature selection techniques are introduced in literature and shows better classification performance (Sharif, Tanvir, Munir, Khan, & Yasmin, 2018). The extracted features consist of several factors that affect the recognition accuracy of the proposed system. The major factors are redundant, irrelevant, and

FIGURE 7 Proposed labeled results on dermoscopy images [Color figure can be viewed at wileyonlinelibrary.com]



noisy information (Khan et al., 2018; Sharif, Khan, Faisal, Yasmin, & Fernandes, 2018). The computational cost of automated systems is quite important (Sharif, Khan, Iqbal, et al., 2018). Therefore, in this work, our major aim for the selection of optimal features is to improve recognition accuracy and reduce computational time (Liaqat et al., 2018). For this purpose, intelligent optimization is required to resolve the problems of redundant, irrelevant, and noisy information. In this work, we implement a BGO algorithm for features optimization. In the BGO algorithm, features are represented by individuals, and each individual updates its position based on the current and target positions of all features. The positions of all features are computed as follows:

$$\chi_i^d = c \left(\sum_{j=1, j \neq i}^N c \frac{ub_d - lb_d}{2} s(|x_j^d - x_i^d|) \frac{x_j - x_i}{d_{ij}} \right) + T_d \quad (30)$$

where ub_d denotes upper bound of features dimension denotes by d^d , lb_d represent lower bound feature, T_d denotes the target value of feature vector, c denotes decreasing coefficient utilized for shrink the comfort zone, and s is social weight defined as $d_{ij} = |x_j - x_i|$. To change the position of individuals, sigmoid transfer function is employed:

$$\Delta \chi = c \left(\sum_{j=1, j \neq i}^N c \frac{ub_d - lb_d}{2} s(|x_j^d - x_i^d|) \frac{x_j - x_i}{d_{ij}} \right) + T(\chi) \quad (31)$$

where $T(\chi) = \frac{1}{1+e^{-\Delta \chi}}$. Finally, the positions of extracted features are updated as:

$$\chi_{t+1}^k(t+1) = \begin{cases} 1 & \text{if } r \text{ and } < T(A\chi(t)+1) \\ 0 & \text{Otherwise} \end{cases} \quad (32)$$

Hence, the fitness function is utilized in this work is:

$$\text{Fit} = \alpha \gamma_R(D) + \beta \frac{|R|}{|N|} \quad (33)$$

where $\gamma_R(D)$ denotes classification error, $|R|$ denotes selected features, $|N|$ represents total fused features, and α, β are random parameters, utilized in selection process. Through BGHO algorithm, the selected best selected features are fed to multiclass SVM of kernel function cubic, quadratic, Gaussian, and linear. The recognition results of M-SVM on selected kernel functions are also compared with few other classification methods as KNN and DT. The few labeled results are shown in Figure 7.

4 | EXPERIMENTAL RESULTS AND ANALYSIS

4.1 | Data sets

In this work, we utilized three publically available data sets of dermoscopy images for evaluating the proposed system. The ISBI 2016 and 2017 data sets are provided by ISIC, and they include 1,279 and 2,750 dermoscopic images, respectively. The ISBI 2016 data set includes 273 malignant and 1,006 benign RGB images with sizes of 542×718 to $2,848 \times 4,288$. The ISBI 2017 data set includes 517 malignant and 2,233 benign 8-bit RGB images. Further, we utilized the PH2 data set for evaluating our system for segmentation and classification. The PH2 data set contains 200 RGB

images comprising 80 common nevi, 80 atypical nevi, and 40 melanomas. The images of the PH2 data set are of a fixed size of 560 × 768.

4.2 | Evaluation metrics

The output of the proposed system is in a binary and labeled form. Two parameters are calculated for evaluating the proposed segmentation process, that is, accuracy and FN rate. Accuracy is computed by comparing a segmented lesion with the corresponding ground truth images of ISBI 2016 and PH2. These ground truth images are generated by expert dermatologists and publicly available for research purposes (Jafari et al., 2017; Mendonça, Ferreira, Marques, Marcal, & Rozeira, 2013). Seven parameters are calculated for classification, that is, accuracy (ACC), area under the curve (AUC), FNR, precision, sensitivity, specificity, and classification time in seconds.

4.3 | Segmentation results

In this step, we analyze the effects of key components on proposed system for lesion segmentation. The key component, which is utilized in this work is size of images. In this work, we select two different image sizes as 256 × 256 and 512 × 512 for image segmentation. The major aim of this process is to analyze the segmentation accuracy when the input images have different dimensions. The segmentation results for PH2 data set are presented in Table 1. In Table 1, the

accuracy results of top 20 images are provided for both image dimensions which show that increase in the image size improves the segmentation accuracy. The average accuracy for image size 256 × 256 is 92.93% with error rate 7.07%. Whereas, for image size 512 × 512, the average accuracy is 93.79% with average error rate 6.21%. The segmentation results of PH2 are also compared with existing methods such as (Pennisi et al., 2016) and (Pathan, Prabhu, & Siddalingaswamy, 2018) which shows that proposed method perform superior.

Second, the ISBI 2016 data set is utilized for segmentation accuracy. As PH2 data set, two different image size strategies are performed as 256 × 256 and 512 × 512. The results are presented in Table 2 that describes that the average accuracy for ISBI 2016 data set is 93.98% using image size 256 × 256. But when image size is increased to 512 × 512, then average segmentation accuracy is reached up to 96.04%. The proposed accuracy is also compared with recent articles that are utilized ISBI 2016 data set such as (Yuan et al., 2017) and (Yu, Chen, Dou, Qin, & Heng, 2017) which shows that the proposed system perform superior. In (Yuan et al., 2017) reported segmentation accuracy 95.5% using ISBI 2016 data set whereas in (Yu, Chen, et al., 2017) achieved accuracy is 94.9%.

4.4 | Classification results

In this section, the detailed classification results are presented in terms of several performance measures, as described in Section 4.2.

TABLE 1 Segmentation results for PH2 data set on different key components

Image size 256 × 256			Image size 512 × 512		
Image no	Accuracy (%)	FNR (%)	Image no	Accuracy (%)	FNR (%)
1	92.42	7.58	1	92.57	7.43
2	92.47	7.53	2	92.78	7.22
3	92.59	7.41	3	92.81	7.19
4	92.60	7.40	4	92.98	7.02
5	92.77	7.23	5	93.02	6.98
6	92.93	7.07	6	93.19	6.81
7	93.11	6.89	7	93.37	6.63
8	93.28	6.72	8	94.14	5.86
9	93.74	6.26	9	94.31	5.69
10	93.89	6.11	10	94.49	5.51
11	94.01	5.99	11	94.87	5.13
12	94.09	5.91	12	94.92	5.08
13	94.22	5.78	13	95.01	4.99
14	94.57	5.43	14	95.76	4.24
15	94.69	5.31	15	95.98	4.02
16	95.55	4.45	16	96.49	3.51
17	95.82	4.18	17	96.97	3.03
18	96.67	3.33	18	97.82	2.18
19	96.95	3.05	19	97.91	2.09
20	97.04	2.96	20	98.19	1.81
Average (all)	92.93	7.07	Average (all)	93.79	6.21

TABLE 2 Segmentation results on ISBI 2016 data set

Image size 256 x 256			Image size 512 x 512		
Image no	Accuracy (%)	FNR (%)	Image no	Accuracy (%)	FNR (%)
1	91.47	8.53	1	92.51	7.49
2	91.53	8.47	2	93.12	6.88
3	91.58	8.42	3	93.87	6.13
4	91.87	8.13	4	94.89	6.19
5	92.07	7.93	5	95.05	4.95
6	92.41	7.59	6	95.41	4.59
7	93.79	6.21	7	95.72	4.28
8	93.86	6.14	8	95.93	4.07
9	93.96	6.04	9	95.97	4.03
10	94.09	5.91	10	95.99	4.01
11	94.21	5.79	11	96.17	3.83
12	94.66	5.34	12	96.29	3.71
13	94.97	5.03	13	96.89	3.11
14	95.03	4.97	14	96.93	3.07
15	95.19	4.81	15	97.78	2.22
16	95.42	4.58	16	98.21	1.79
17	95.92	4.08	17	98.14	1.86
18	96.01	3.99	18	97.46	2.54
19	96.19	3.81	19	98.01	1.99
20	97.59	2.41	20	98.39	1.61
Average (all)		93.98	Average (all)		96.04
		6.02			5.96

TABLE 3 Classification results for ISBI 2016 data set using different decision tree methods

MH	Decision tree methods			Performance metrics						
	GDI	TW	MDR	Acc (%)	AUC	FNR (%)	Prec (%)	Sen (%)	Spec (%)	Time (s)
1	✓			78.5	0.79	21.8	79.0	78.5	70.0	30.5
		✓		78.2	0.79	21.8	79.0	78.5	70.0	32.5
			✓	81.6	0.82	18.4	82.5	82.0	75.0	28.6
2	✓			78.5	0.79	21.5	79.0	78.5	73.0	7.8
		✓		78.5	0.79	21.5	79.0	78.5	73.0	7.8
			✓	79.2	0.70	20.8	79.0	78.5	73.0	7.8
Proposed	✓			84.4	0.86	15.6	85.5	84.0	75.0	5.4
		✓		84.4	0.86	15.6	85.5	84.5	75.0	5.8
			✓	83.3	0.84	16.7	84.5	83.0	75.0	5.6

Note: Acc represents accuracy, Prec denotes the precision rate, Sen represents sensitivity, and Spec denotes specificity.

The ISBI 2016, ISBI 2017, and PH2 data sets are utilized. The classification results are evaluated in the following three steps: (a) fusion of OCL and OHOG features (PHOG-OCL); (b) fusion of OCL, OHOG, and GLCM features (OPHG-OCL-GL); (c) OFS. A 70:30 approach is adopted, in which 70% of the images in the data sets are used for training the system and the remaining 30% are employed for testing. Ten-fold cross validation is performed for classification, in which the testing features set is divided into 10 subsets. Each set contains almost the same number of benign and melanoma lesions. Nine sets

are utilized for training and the remaining one is used for testing. The final results are the average of all 10 sets.

4.4.1 | ISBI 2016 classification results

The classification results of the ISBI 2016 data set obtained using different DT methods are presented in Table 3. The DT methods that are utilized in this work are the Gini diversity index (GDI), towing rule (TW), and maximum deviance reduction (MDR). Method 1 explains

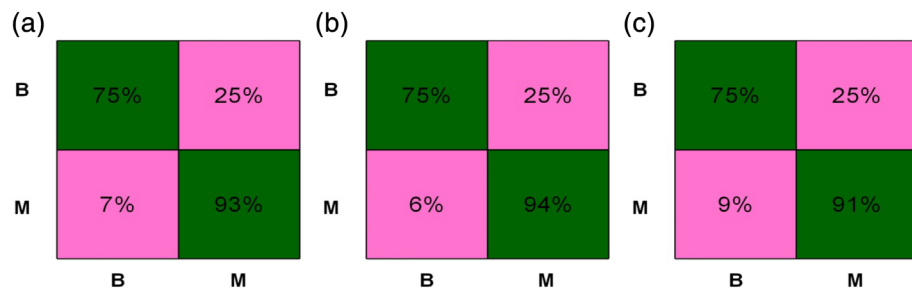


FIGURE 8 Confusion matrix for ISBI 2016 data set using decision tree with different kernel functions. (a) Gini diversity index, (b) towing rule, and (c) max deviance reduction [Color figure can be viewed at wileyonlinelibrary.com]

TABLE 4 Classification results for ISBI 2016 data set using different SVM methods

MH	SVM methods				Performance measures						
	Gaussian	Linear	Quad	Cubic	Acc (%)	AUC	FNR	Prec	Sen (%)	Spec (%)	Time (s)
1	✓				87.1	0.96	12.9	87.0	87.0	84	43.5
		✓			82.0	0.88	12.9	82.5	82.0	77	32.1
			✓		86.4	0.94	18.0	86.5	86.5	82	53.5
				✓	87.5	0.95	12.5	87.5	87.5	84	36.5
2	✓				86.8	0.95	12.5	86.5	86.5	83	53.6
		✓			80.7	0.88	13.5	81.0	81.0	75	72.8
			✓		84.5	0.93	19.3	85.0	84.5	79	61.6
				✓	86.1	0.95	15.5	86.0	86.0	82	39.7
Proposed	✓				93.8	0.99	6.2	94.0	93.5	99	4.8
		✓			90.5	0.96	9.5	91.0	90.5	86	6.3
			✓		91.8	0.97	9.5	92.0	92.0	90	7.9
				✓	93.4	0.97	6.6	94.4	94.5	96	5.1

Note: Sen denotes sensitivity, spec represents specificity, Prec shows precision.

the PHOG-OCL features that are utilized for classification, and a maximum accuracy of 81.6% is obtained using the MDR method. The AUC, FNR, precision, sensitivity, and specificity are 0.82, 18.4, 82.5, 82, and 75%, respectively. The classification computation time for the MDR method is 28.6 s, which is better compared to the GDI and TW approaches. Method 2 explains the OPHG-OCL-GL features that are used for classification. The maximum achieved accuracy is 79.2% for the MDR method, which is less compared to Method 1, but the computational time is improved to 7.8 s. Finally, the proposed OFS method is utilized for classification, as presented in Table 3. The selected features perform well in the case of the GDI and TW methods and an accuracy of 84.4% is achieved. The computational times of the GDI and TW methods are 5.4 s each. The classification performance of the proposed selection approach on the ISBI 2016 data set is also verified by the confusion matrices given in Figure 8.

The classification results obtained using advanced SVM methods are presented in Table 4. Four different kernel functions are employed for obtaining classification results, that is, Gaussian, linear, quadratic, and cubic. Three different features strategies are utilized for classification, that is, as PHOG-OCL, OPHG-OCL-GL, and OFS. In the first strategy, PHOG-OCL features are used, and a maximum classification accuracy of 87.5% is achieved on the cubic kernel function. The AUC, FNR, precision, sensitivity, and specificity are 0.95, 12.5, 87.5, 87.5,

and 84%, respectively. Computational time is also calculated for all methods, and the best time is 32.1 s for the linear kernel function.

In the second strategy, OPHG-OCL-GL features are used for classification, and a maximum classification accuracy of 86.8% is obtained for the Gaussian kernel function. Classification accuracies of 80.7, 84.5, and 86.1% are obtained for the linear, quadratic, and cubic functions, respectively. It should be noted that the fusion of OPHG-OCL-GL features increases computational time compared to OPHG-OCL feature sets.

Finally, the proposed optimal features are used for classification. The maximum classification accuracy is 93.8% for the Gaussian SVM function. The AUC, FNR, precision, sensitivity, and specificity are 0.99, 6.2, 94.0, 93.5, and 99%, respectively. The SVM exhibits good performance for the linear, quadratic, and cubic kernel functions, with accuracies of 90.5, 91.8, and 93.4%, respectively. The computational time of the Gaussian kernel function is 4.8 s, which is significantly improved compared to the OPHG-OCL and OPHG-OCL-GL feature sets. The classification accuracy of OFS for all kernel functions is also presented in the confusion matrices given in Figure 9.

Fine K-NN classification results using different kernel functions such as correlation, Hamming, Cosine, and Spearman are presented in Table 5. The results are computed for each feature sets such as OPHG-OCL, OPHG-OCL-GL, and optimal feature selection. The best classification accuracy for OPHG-OCL feature set is 90.1% on

FIGURE 9 Confusion matrix for ISBI 2016 data set using SVM with different kernel functions. (a) Gaussian, (b) linear, (c) quadratic, and (d) cubic function [Color figure can be viewed at wileyonlinelibrary.com]

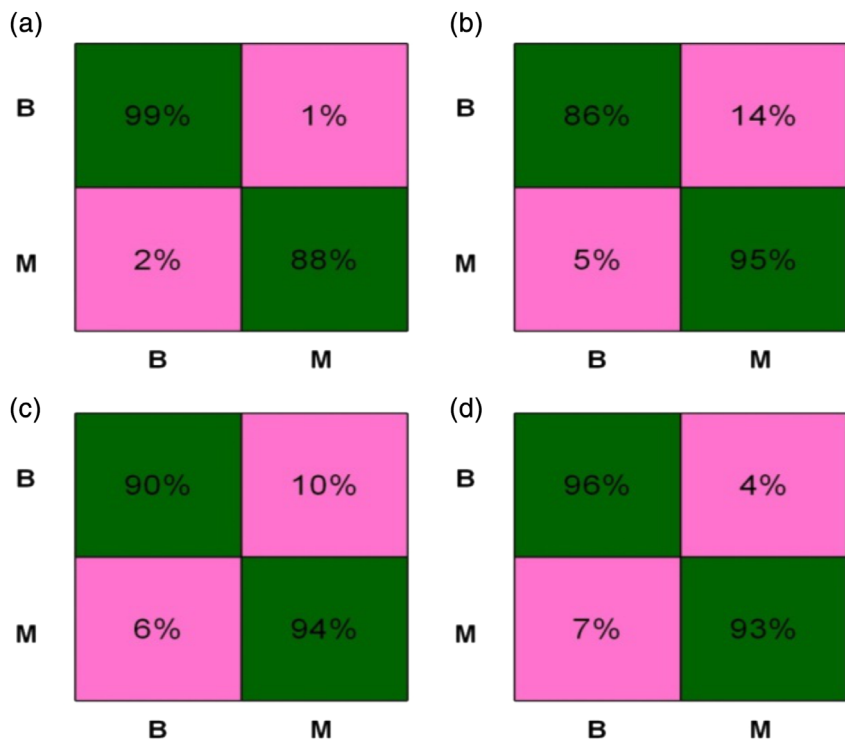


TABLE 5 Classification results for ISBI 2016 data set using different KNN methods

MH	K-nearest neighbor methods				Performance measures						
	Corr	Hamming	Cosine	Spearman	Acc (%)	AUC	FNR	Prec (%)	Sen (%)	Spec (%)	Time (s)
1	✓				80.4	0.87	19.6	81.0	80.5	87.0	24.0
		✓			90.1	0.90	9.9	91.0	90.5	98.0	37.5
			✓		86.3	0.86	13.7	87.0	86.5	82.0	43.8
				✓	80.3	0.86	19.7	81.0	80.5	87.0	26.3
2	✓				77.3	0.84	22.7	78.0	77.5	85.0	44.1
		✓			78.0	0.90	22.0	84.5	77.5	99.0	53.6
			✓		77.1	0.84	22.9	77.5	77.0	85.0	54.1
				✓	77.8	0.84	22.2	78.5	78.0	84.0	55.1
Proposed	✓				82.4	0.89	17.6	82.5	82.5	83.0	19.6
		✓			77.5	0.84	22.5	77.5	77.5	76.0	16.2
			✓		82.3	0.89	17.7	82.5	82.5	82.0	10.1
				✓	82.5	0.89	17.5	82.5	82.5	83.0	14.1

Note: Acc denotes accuracy, Corr denotes correlation, Spec denotes specificity.

Abbreviation: KNN, K-nearest neighbors.

Hamming fitness function of KNN, whereas the 82.7% accuracy is achieved on 78% on Hamming fitness function for feature set OPHG-OCL-GL. The best classification accuracy for proposed optimal feature selection approach is 82.5% on Spearman fitness function. The other function as correlation, Hamming, and Cosine are achieved accuracy 82.4, 77.5, and 82.3%, respectively. The classification results for optimal feature selection are also verified by confusion matrices in Figure 10. In addition, the computational cost for each method is calculated as given in Table 5 which explains that when increase in the number of features, the system execution is also increased but for

selection approach, the execution time is minimized which is good for any real time CAD system.

4.4.2 | ISBI 2017 classification results

The classification results obtained for the ISBI 2017 data set are presented in this section. The classification results for the advanced SVM methods are presented in Table 6. Four different kernel functions are utilized, that is, Gaussian, linear, quadratic, and cubic. The results are obtained for all functions using different feature strategies. PHOG-

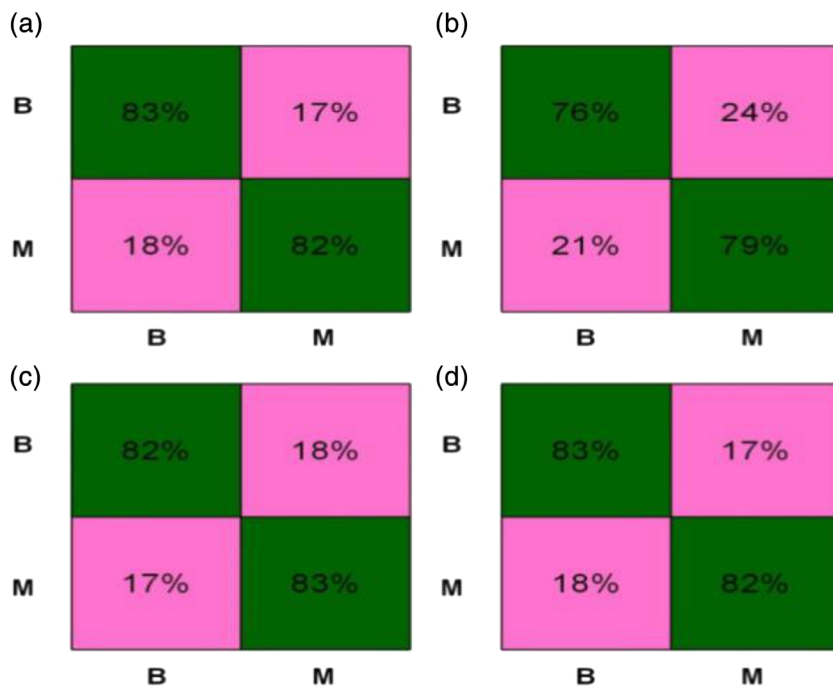


FIGURE 10 Confusion matrix for ISBI 2016 data set using K-nearest neighbor classifier with different kernel functions. (a) Correlation, (b) hamming, (c) cosine, and (d) spearman function [Color figure can be viewed at wileyonlinelibrary.com]

TABLE 6 Classification results for ISBI 2017 data set using different SVM methods

MH	SVM methods				Performance measures						
	Gaussian	Linear	Quad	Cubic	Acc (%)	AUC	FNR	Prec (%)	Sensitivity (%)	Spec (%)	Time (s)
1	✓				72.1	0.72	27.9	70.5	70.0	63.0	58.29
		✓			68.6	0.66	31.4	71.0	64.0	46.0	56.11
			✓		72.7	0.74	27.3	70.5	69.5	54.0	52.97
				✓	88.9	0.97	11.1	89.0	89.0	84.0	50.09
2	✓				90.6	0.96	9.4	90.5	90.5	91.0	43.82
		✓			86.2	0.87	13.8	86.5	86.0	85.0	82.32
			✓		86.7	0.88	13.3	87.0	86.5	88.0	41.92
				✓	84.5	0.86	15.4	84.5	84.5	87.0	31.28
Proposed	✓				93.7	0.97	6.3	94.1	93.3	95.0	38.61
		✓			92.2	0.97	7.8	92.0	92.0	92.0	31.51
			✓		89.2	0.95	10.8	89.5	86.5	92.0	26.00
				✓	84.4	0.85	15.6	84.5	84.5	83.0	28.62

Note: Acc denotes accuracy, Corr denotes correlation, Prec denotes precision value, Spec denotes specificity.

OCL features are used in the first strategy, and the maximum classification accuracy, sensitivity, precision, precision rate, and minimum classification time are 88.9%, 89%, 89%, 84%, and 50.09 s for the cubic kernel function, respectively.

In the second strategy, classification is performed on OPHG-OCL-GL features. The maximum classification accuracy, sensitivity, precision, and specificity are 90.6, 90.5, 90.5, and 91% for the Gaussian kernel function. Execution time is calculated for each kernel function, and the minimum execution time is 31.28 s, which is better compared to OPHG-OCL features.

Finally, classification results are computed using the proposed BGO algorithm, and high performance is observed in terms of accuracy, precision rate, sensitivity, specificity, and AUC, whose values are

93.7, 94.1%, 93.3, 95.0, and 0.97%, respectively, as presented in Table 6. The accuracies obtained on linear, quadratic, and cubic functions are 92.2, 89.2, and 84.4%, respectively. The classification accuracy of all SVM functions is also presented in the form of confusion matrix in Figure 11. In addition, execution time is computed for all functions, and the best time is 26.0 s for the quadratic function. The execution time of the BGO algorithm is significantly better compared to PHOG-OCL and OPHG-OCL-GL features.

4.5 | Discussion and comparison

The detail discussion of segmentation and classification results is presented in this section in the form of numerical. As shown in Figure 2,

FIGURE 11 Confusion matrix of ISBI 2017 using SVM methods. (a) Gaussian function, (b) linear function, (c) quadratic function, and (d) cubic function [Color figure can be viewed at wileyonlinelibrary.com]

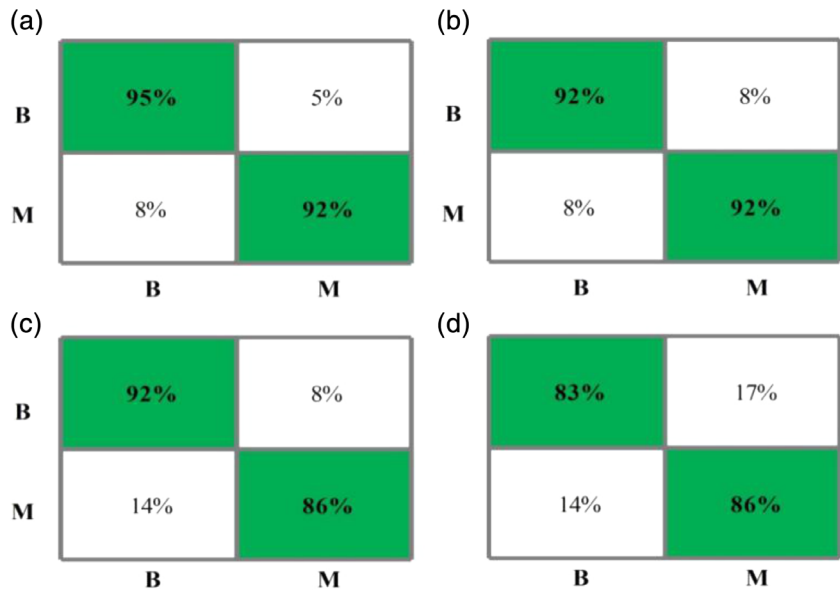


TABLE 7 Proposed segmentation comparison with recent techniques

Method	Year	Data set	Accuracy
[38]	2018	PH2	93.4%
[37]	2016	PH2	89.6%
[45]	2017	PH2	90.25%
Proposed	2019	PH2	93.79%
[17]	2017	ISBI2016	95.5%
[39]	2017	ISBI2016	94.9%
[37]	2016	ISBI2016	91.18%
[46]	2017	ISBI2016	92.3%
[38]	2018	ISBI2016	94.6%
Proposed	2019	ISBI2016	96.04%

the proposed automated method follows the sequence from lesion contrast enhancement to classification. In the first phase, the segmentation accuracy is computed as presented for PH2 and ISBI2016 data sets as presented in Tables 1 and 2. The visual segmentation effects are also shown in Figures 5 and 7. Later, a comparison is conducted with recent techniques, given in Table 7. The results show the superiority of proposed technique.

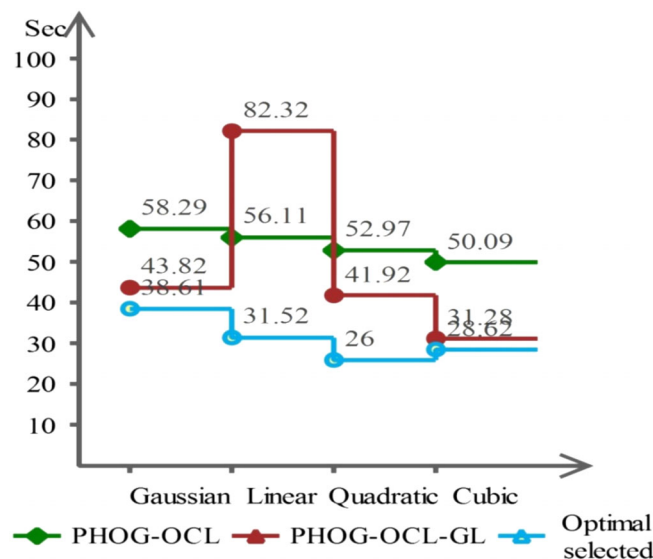
In the second phase, the classification accuracy is computed and results are presented in Tables 3–6. The proposed classification accuracy is also verified through Figures 8–11. Later, a classification comparison of propose results is also conducted in the Table 8. The classification results are compared based on five performance metrics, that is, accuracy, specificity, AUC, sensitivity, and classification time. Lopez, Giro-i-Nieto, Burdick, and Marques (2017) presented a deep learning approach for skin cancer classification and achieved a sensitivity of 78.66%, a precision of 79.74%, and an accuracy of 81.33% for the ISBI 2016 data set. Yu, Jiang, Wang, and Lei (2017) introduced an aggregating CNN method for

melanoma classification and reported a sensitivity of 42.60%, a specificity of 97.70%, an AUC of 85.20%, and an accuracy of 86.80%. Yu, Chen, et al. (2017) implemented a deep residual method for melanoma recognition from dermoscopy images and achieved a sensitivity rate of 50.70%, a specificity of 93.0%, an AUC of 85.0%, and an accuracy of 93.80%. In recent years, Khan et al. (2018) implemented an optimized method for lesion classification and achieved an accuracy of 83.20. The few other methods such as Khan et al. (2019) and Sharma and Bhave (2019) achieved an accuracy of 89.2 and 75%, respectively. The proposed method achieves a sensitivity of 93.50%, a specificity of 99%, a precision of 94.00%, an AUC of 0.99, an accuracy of 93.80%, and a classification time of 4.8 s for the ISBI 2016 data set. The results show that the proposed system exhibits superior performance compared to existing methods.

The comparison of classification results for the ISBI 2017 data set is also presented in Table 8. Khan et al. reported an accuracy of 88.5%, a sensitivity rate of 88.50%, a specificity of 91.0%, and an AUC of 93.0%, respectively (Khan et al., 2018). Sultana, Mandal, and Puhan (2018) introduced an approach for skin lesion classification and evaluated it using the ISBI 2017 data set. They reported a classification accuracy of 83.2%, a sensitivity rate of 83.20%, a specificity of 90.55%, and an AUC 78.9%. Recently, Sarker et al. (2018) achieved an accuracy of 93.6% on ISBI2017 data set. The proposed method achieved a classification accuracy of 93.70%, a sensitivity of 93.30%, a specificity of 95.0%, and an AUC of 97%. In addition, classification execution time was computed for all three strategies using four SVM kernel functions and plotted in Figure 12. The figure shows that the fusion of PHOG, OCL, and GL features increases execution time. However, after OFS, execution time reduces to 26 (s). The results show that the proposed system outperforms existing methods in terms of classification time and accuracy on the ISBI 2017 data set.

TABLE 8 Comparison with existing techniques for ISBI 2016 and ISBI 2017

Method	Data set	Measures					
		Sensitivity (%)	Specificity (%)	Precision (%)	AUC	Accuracy (%)	Time (s)
[40]	ISBI 2016	78.66	-	79.74	-	81.33	-
[41]	ISBI 2016	42.60	97.70	-	85.20	86.80	-
[39]	ISB 2016	50.70	94.10	-	80.40	85.10	-
[1]	ISBI 2016	75.50	93.00	-	85.00	83.20	-
[16]	ISBI 2016	89.0	87.0	89.0	0.96	89.2	-
[42]	ISBI 2016	-	-	-	-	75.0	-
[1]	ISBI 2017	88.50	91.0	-	93.0	88.5	-
[43]	ISBI 2017	83.20	90.5	-	78.9	83.2	-
[44]	ISBI 2017	-	-	-	-	93.60	-
Proposed	ISBI 2016	93.50	99.00	94.00	0.99	93.80	4.80
Proposed	ISBI 2017	93.30	95.00	94.10	0.97	93.70	38.61

**FIGURE 12** Graphical comparison of classification time of selected features strategies [Color figure can be viewed at wileyonlinelibrary.com]

5 | CONCLUSION

A new automated method is proposed for skin lesion recognition based on normal distribution and optimal feature selection. A brighter channel contrast stretching approach is proposed, which makes the lesion region more visible. Good lesion contrast is helpful for accurate lesion segmentation. After lesion segmentation, OHOG, OCL, and GLCM texture analysis features are extracted. The extracted features are fused through a covariance-based approach. Finally, a BGO algorithm is implemented on fused features and an optimal feature vector is obtained as the output. The obtained optimal feature vector is finally classified using an SVM. It is also observed that the poor contrast lesion images not only affect segmentation accuracy but also affect good feature extraction. Weak features diminish classification

accuracy. Moreover, the fusion of multiple features enhances classification accuracy; however, execution time is doubled. Therefore, we conclude that the OFS algorithm not only improves classification accuracy but also minimizes execution time.

The proposed system is validated on the ISBI 2016, ISBI 2017, and PH2 data sets, and it exhibits notable performance. In addition, the proposed system is compared with existing approaches for validation and demonstrating the superiority of the system. The overall average segmentation and classification results are superior as compared to existing methods. In future, we will work on a deep learning method and use more data sets and evaluation parameters. In addition, we promote this application for clinical practices, as it may be helpful for doctors in the diagnosis process.

ORCID

Muhammad Sharif <https://orcid.org/0000-0002-6347-4890>

Amjad Rehman <https://orcid.org/0000-0002-3817-2655>

REFERENCES

- Akram, T., Khan, M. A., Sharif, M., & Yasmin, M. (2018). Skin lesion segmentation and recognition using multichannel saliency estimation and M-SVM on selected serially fused features. *Journal of Ambient Intelligence and Humanized Computing*, 1–20.
- Alfed, N., & Khelifi, F. (2017). Bagged textural and color features for melanoma skin cancer detection in dermoscopic and standard images. *Expert Systems with Applications*, 90, 101–110.
- Bakheet, S. (2017). An SVM framework for malignant melanoma detection based on optimized hog features. *Computation*, 5(1), 4.
- Barata, A. C. F., Celebi, E. M., & Marques, J. (2018). A survey of feature extraction in Dermoscopy image analysis of skin cancer. *IEEE Journal of Biomedical and Health Informatics*.
- Dey, N., Rajinikanth, V., Ashour, A., & Tavares, J. M. (2018). Social group optimization supported segmentation and evaluation of skin melanoma images. *Symmetry*, 10(2), 51.
- Jafari, M. H., Nasr-Esfahani, E., Karimi, N., Soroushmehr, S. R., Samavi, S., & Najarian, K. (2017). Extraction of skin lesions from non-

- dermoscopic images for surgical excision of melanoma. *International Journal of Computer Assisted Radiology and Surgery*, 12(6), 1021–1030.
- Khan, M. A., Akram, T., Sharif, M., Javed, M. Y., Muhammad, N., & Yasmin, M. (2019). An implementation of optimized framework for action classification using multilayers neural network on selected fused features. *Pattern Analysis and Applications*, 1–21.
- Khan, M. A., Akram, T., Sharif, M., Saba, T., Javed, K., Lali, I. U., ... Rehman, A. (2019). Construction of saliency map and hybrid set of features for efficient segmentation and classification of skin lesion. *Microscopy Research and Technique*, 82, 741–763.
- Khan, M. A., Akram, T., Sharif, M., Shahzad, A., Aurangzeb, K., Alhussein, M., ... Altamrah, A. (2018). An implementation of normal distribution based segmentation and entropy controlled features selection for skin lesion detection and classification. *BMC Cancer*, 18(1), 638.
- Khan, M. A., Lali, I. U., Rehman, A., Ishaq, M., Sharif, M., Saba, T., ... Akram, T. (2019). Brain tumor detection and classification: A framework of marker-based watershed algorithm and multilevel priority features selection. *Microscopy Research and Technique*, 82, 909–922.
- Khan, M. A., Sharif, M., Javed, M. Y., Akram, T., Yasmin, M., & Saba, T. (2017). License number plate recognition system using entropy-based features selection approach with SVM. *IET Image Processing*, 12(2), 200–209.
- Kimball, T. G. (2018). Is cancer a moral failing? What About Addiction? Why cancer treatment protocols can help destigmatize addiction and improve outcomes. *Young*.
- Koh, H. K., Geller, A. C., Miller, D. R., Grossbart, T. A., & Lew, R. A. (1996). Prevention and early detection strategies for melanoma and skin cancer: Current status. *Archives of Dermatology*, 132(4), 436–443.
- Kumar, V., & Choudhury, T. (2019). Real-time recognition of malignant skin lesions using ensemble modeling.
- Liaqat, A., Khan, M. A., Shah, J. H., Sharif, M., Yasmin, M., & Fernandes, S. L. (2018). Automated ulcer and bleeding classification from wce images using multiple features fusion and selection. *Journal of Mechanics in Medicine and Biology*, 18(04), 1850038.
- Lopez, A. R., Giro-i-Nieto, X., Burdick, J., & Marques, O. (2017). Skin lesion classification from dermoscopic images using deep learning techniques. Paper presented at the 2017 13th IASTED International Conference on Biomedical Engineering (BioMed). Innsbruck, Austria
- Mahmoud, H., Abdel-Nasser, M., & Omer, O. A. (2018). Computer aided diagnosis system for skin lesions detection using texture analysis methods. Paper presented at the 2018 International Conference on Innovative Trends in Computer Engineering (ITCE). Egypt Aswan
- Masood, A., & Al-Jumaily, A. (2018). Orientation sensitive fuzzy C means based fast level set evolution for segmentation of histopathological images to detect skin cancer. Paper presented at the International Conference on Hybrid Intelligent Systems. Porto, Portugal
- Mendonça, T., Ferreira, P. M., Marques, J. S., Marcal, A. R., & Rozeira, J. (2013). PH 2-A dermoscopic image database for research and benchmarking. Paper presented at the 2013 35th Annual International Conference of the IEEE Engineering in Medicine and Biology Society (EMBC). Osaka, Japan
- Mirikhraji, Z., & Hamarneh, G. (2018). Star shape prior in fully convolutional networks for skin lesion segmentation. *arXiv*, 1806, 08437.
- Nasir, M., Attique Khan, M., Sharif, M., Lali, I. U., Saba, T., & Iqbal, T. (2018). An improved strategy for skin lesion detection and classification using uniform segmentation and feature selection based approach. *Microscopy Research and Technique*, 81, 528–543.
- Navarro, F., Escudero-Vinolo, M., & Bescos, J. (2018). Accurate segmentation and registration of skin lesion images to evaluate lesion change. *IEEE Journal of Biomedical and Health Informatics*.
- Nida, N., Irtaza, A., Javed, A., Yousaf, M. H., & Mahmood, M. T. (2019). Melanoma lesion detection and segmentation using deep region based convolutional neural network and fuzzy C-means clustering. *International Journal of Medical Informatics*, 124, 37–48.
- Norouzi, A., Rahim, M. S. M., Altameem, A., Saba, T., Rada, A. E., Rehman, A., & Uddin, M. (2014). Medical image segmentation methods, algorithms, and applications. *IETE Technical Review*, 31(3), 199–213. <https://doi.org/10.1080/02564602.2014.906861>
- Ondimu, S., & Murase, H. (2008). Effect of probability-distance based Markovian texture extraction on discrimination in biological imaging. *Computers and Electronics in Agriculture*, 63(1), 2–12.
- Pathan, S., Prabhu, K. G., & Siddalingaswamy, P. (2018). Hair detection and lesion segmentation in dermoscopic images using domain knowledge. *Medical & Biological Engineering & Computing*, 1–15.
- Pennisi, A., Bloisi, D. D., Nardi, D., Giampetrucci, A. R., Mondino, C., & Facchiano, A. (2016). Skin lesion image segmentation using Delaunay Triangulation for melanoma detection. *Computerized Medical Imaging and Graphics*, 52, 89–103.
- Rogers, H. W., Weinstock, M. A., Feldman, S. R., & Coldiron, B. M. (2015). Incidence estimate of nonmelanoma skin cancer (keratinocyte carcinomas) in the US population, 2012. *JAMA Dermatology*, 151(10), 1081–1086.
- Saba, T., Al-Zahrani, S., & Rehman, A. (2012). Expert system for offline clinical guidelines and treatment. *Life Sci Journal*, 9(4), 2639–2658.
- Sarker, M., Kamal, M., Rashwan, H. A., Banu, S. F., Saleh, A., Singh, V. K., ... Radeva, P. (2018). SLSDeep: Skin lesion segmentation based on dilated residual and pyramid pooling networks. *arXiv*.
- Sharif, M., Khan, M. A., Akram, T., Javed, M. Y., Saba, T., & Rehman, A. (2017). A framework of human detection and action recognition based on uniform segmentation and combination of Euclidean distance and joint entropy-based features selection. *EURASIP Journal on Image and Video Processing*, 2017(1), 89.
- Sharif, M., Khan, M. A., Faisal, M., Yasmin, M., & Fernandes, S. L. (2018). A framework for offline signature verification system: Best features selection approach. *Pattern Recognition Letters*.
- Sharif, M., Khan, M. A., Iqbal, Z., Azam, M. F., Lali, M. I. U., & Javed, M. Y. (2018). Detection and classification of citrus diseases in agriculture based on optimized weighted segmentation and feature selection. *Computers and Electronics in Agriculture*, 150, 220–234.
- Sharif, M., Tanvir, U., Munir, E. U., Khan, M. A., & Yasmin, M. (2018). Brain tumor segmentation and classification by improved binomial thresholding and multi-features selection. *Journal of Ambient Intelligence and Humanized Computing*, 1–20.
- Sharma, M., & Bhavate, A. (2019). Lesion classification using convolutional neural network. In J. Wang, G. R. M. Reddy, V. K. Prasad, & V. S. Reddy (Eds.), *Soft Computing and Signal Processing* (pp. 357–365). US: Springer.
- Siegel, R. L., Miller, K. D., & Jemal, A. (2018). Cancer statistics, 2018. *CA Cancer Journal for Clinicians*, 68, 7–30.
- Sultana, N. N., Mandal, B., & Puhan, N. (2018). Deep residual network with regularised fisher framework for detection of melanoma. *IET Computer Vision*, 12, 1096–1104.
- Ullah, H., Saba, T., Islam, N., Abbas, N., Rehman, A., Mehmood, Z., & Anjum, A. (2019). An ensemble classification of exudates in color fundus images using an evolutionary algorithm based optimal features selection. *Microscopy Research and Technique*. <https://doi.org/10.1002/jemt.23178>
- Vasicek, B. E., Szpunar, S. M., & Manz-Dulac, L. A. (2018). Patient knowledge of sunscreen guidelines and frequency of physician counseling: A cross-sectional study. *The Journal of Clinical and Aesthetic Dermatology*, 11(1), 35–40.
- Vesal, S., Patil, S. M., Ravikumar, N., & Maier, A. (2018). A multi-task framework for skin lesion detection and segmentation. *arXiv*.
- Xian, G.-m. (2010). An identification method of malignant and benign liver tumors from ultrasonography based on GLCM texture features and fuzzy SVM. *Expert Systems with Applications*, 37(10), 6737–6741.

- Yu, L., Chen, H., Dou, Q., Qin, J., & Heng, P.-A. (2017). Automated melanoma recognition in dermoscopy images via very deep residual networks. *IEEE Transactions on Medical Imaging*, 36(4), 994–1004.
- Yu, Z., Jiang, X., Wang, T., & Lei, B. (2017). *Aggregating deep convolutional features for melanoma recognition in dermoscopy images*. Paper presented at the International Workshop on Machine Learning in Medical Imaging.
- Yuan, Y., Chao, M., & Lo, Y.-C. (2017). Automatic skin lesion segmentation using deep fully convolutional networks with jaccard distance. *IEEE Transactions on Medical Imaging*, 36(9), 1876–1886.

How to cite this article: Afza F, Khan MA, Sharif M, Rehman A. Microscopic skin laceration segmentation and classification: A framework of statistical normal distribution and optimal feature selection. *Microsc Res Tech*. 2019;82: 1471–1488. <https://doi.org/10.1002/jemt.23301>